

RADIATION TRANSPORT CALCULATIONS IN TREATMENT PLANNING

Jeffrey F. Williamson

Department of Radiation Oncology, University of Arizona Health Sciences Center, Tucson, AZ 85724

(Received 2 September 1988)

Abstract—This article reviews the role of radiation transport calculations in radiotherapy dose computation. The physical and mathematical principles underlying transport theory, as applied to electrons and photons, are discussed. Practical methods of solving the transport equation, with emphasis on Monte Carlo techniques, are reviewed. The contribution of analytic and Monte Carlo transport calculations to electron beam, photon beam, and brachytherapy treatment planning dosimetry is assessed. Currently, the most important roles of transport theory include using approximate solutions of the transport equation as theoretical foundations of dose computation algorithms, and using Monte Carlo simulation to calculate basic treatment planning data, characteristic of the treatment modality, which can serve as input to a dose computation algorithm.

Key Words: Radiation therapy, Treatment planning, Dosimetry, Monte Carlo, Photon and electron transport

1.0 INTRODUCTION

One of the most exciting current developments in ionizing radiation dosimetry is the application of radiation transport theory to dosimetric problems of clinical interest. In contrast to the highly successful but empirical methods (1, 2) traditionally used to estimate absorbed dose within the patient, transport theory begins with a mathematical description of the scattering and absorption processes underlying energy deposition in matter and a geometric description of the absorbing media and radiation sources around and within the patient. A central result of transport theory is that, in principle, the Boltzmann transport equation can be used to completely characterize the distribution of ionizing radiation and related quantities, such as absorbed dose, within such a system. Recent improvements in the computing speed and central memory supported by modern computers, accuracy of available cross-section data, and numerical methods of solving the transport equation, permit this simulation technology to be applied to many geometrically complex problems of clinical relevance.

The purpose of this article is to review the computational methods of photon and electron transport along with some of their current and potential uses in dosimetric calculation.

2.0 THE NATURE OF RADIATION TRANSPORT

In this section, the transport problem will be described in terms of the integral Boltzmann transport

equation. The Monte Carlo method of solving this equation for electrons and photons will be briefly described.

2.1 Particle fluence and the Boltzmann transport equation

A useful quantity for describing the distribution of photons or electrons within a system of absorbers and sources is the particle fluence, $\Phi(r, \Omega, E)$, which is a function of spatial position r , direction or flight path Ω , and photon energy E . $\Phi(r, \Omega, E)d\Omega dE$ is defined as the ratio dN/dA , where dN is the number of particles which pass through area dA aligned normal to Ω and located at r , such that their directions are confined to a cone of solid angle $d\Omega$ centered about Ω and their energies are confined to the interval $[E, E + dE]$. Thus, Φ has the units of particles per cm^2 per unit solid angle and energy. If $\Phi(r, \Omega, E)$ is integrated over all energies and directions, the resultant quantity is equivalent to particle fluence as defined by the ICRU (3). To simplify formulation of the transport problem, Φ is assumed to be time-independent.

Given the particle fluence, all other dosimetric quantities of interest can, in principle, be computed. For example, assuming that uncharged particles do not directly deposit energy to matter, the absorbed dose to the medium can be estimated as follows (81):

$$D(r) = \int_{\Delta} \int_{4\pi} \Phi(r, \Omega, E) \cdot (L_{\Delta}(E)/\rho) d\Omega dE \\ + \int_{4\pi} \Delta \Phi(r, \Omega, \Delta) \cdot (S_{col}(\Delta)/\rho) d\Omega \quad (1)$$

where Φ denotes particle fluence arising from primary and secondary electrons, (L_{Δ}/ρ) and (S_{col}/ρ) are the restricted and unrestricted mass collisional stopping powers, respectively, and $d\Omega = \sin \theta \cdot d\theta \cdot d\phi$. Δ denotes the cutoff energy below which electrons can be assumed to dissipate or impart their energy locally to the medium. The second term of Eq. 1 is an approximate expression (81) for the residual energy deposited by electrons whose energies fall below Δ near point r .

Four types of elementary physical data are needed to solve the transport equation for any system:

1. The probability of occurrence for each elementary interaction process as a function of incident particle energy E and relevant properties of the absorbing medium. These data are tabulated in terms of cross sections, $\sigma(E, Z, \rho)$, where Z and ρ are the atomic number and mass density of the medium. Equivalently, the linear attenuation coefficient μ can be used. For photons, the relevant cross sections are those describing the familiar photo-electric and pair production absorption processes, and the coherent and incoherent scattering processes. For charged particles (4), the Moller and Bhabha cross sections describe scattering of electrons and positrons, respectively, by orbital electrons. The elastic scattering of electrons or positrons by a nucleus is described by the Mott or the less accurate Rutherford cross section. Finally, for high energy electrons, Bremsstrahlung production is an important mechanism of energy loss.
2. For each of the collisional processes described above, the likelihood of each possible outcome of an interaction, in terms of angle Ω' and energy, E' , of the emergent scattered or secondary particle, must be known. This information is given by the differential cross section, $d^2\sigma(\Omega', E' | \Omega, E)/dE'd\Omega'$ characteristic of the collision process.
3. The probability distribution governing the distances traveled by particles between successive scattering events. This distribution is derived from the exponential attenuation law.
4. In the condensed history approach to Monte Carlo simulation of electron transport, linear stopping powers and multiple scattering distributions are required.

The fluence at each point within a system of ionizing radiation sources and absorbing media is completely determined by the time-invariant Boltzmann transport equation. Several simplifying assumptions (5, 6) are made in deriving this fundamental equation, which allow photon and electron

trajectories to be idealized as zig-zag paths, consisting of straight-line flights between successive collisions with matter which abruptly change the energy and direction of the particle. First, quanta of radiation are assumed to be point particles with well defined positions and energies. Interactions between the radiation field and matter are assumed to occur instantaneously at discrete scattering centers (e.g., atoms and electrons), which occupy precise locations in space. The collision dynamics are assumed to be dominated by very short-range forces relative to the particle mean free path. In addition, quanta of radiation are assumed to interact with one scattering center at a time but not with one another. Thus, quantal effects such as interference and diffraction are ignored. Within this conceptual framework, many phenomena can be accurately described, including the effects of external electric and magnetic fields upon charged particles.

We present only the integral form of the transport equation (7), since it most clearly demonstrates the connection between analytic and Monte Carlo solutions. First, the particle flux is expanded by orders of scattering:

$$\Phi(\beta) = \sum_{j=0}^{\infty} \Phi_j(\beta) \quad (2)$$

where Φ_j is the number of particles per unit area, solid angle, and energy that have been scattered j times and $\beta = (r, \Omega, E)$ where $\Phi_0(\beta)$ denotes the primary particle fluence. The Boltzmann equations, corresponding to each order of scattering, n , are:

$$\begin{aligned} \mu(E, r)\Phi_n(\beta) &= \int \mu(E', r')\Phi_{n-1}(\beta')P(\beta|\beta')d\beta' \quad n \geq 1 \\ \Phi_0(\beta) &= \int_0^{\infty} e^{-\mu R} S(r - R\Omega, \Omega, E) dR \quad n = 0 \end{aligned} \quad (3)$$

where $S(\beta)$, the source distribution function, is the number of primary particles originating at r with energy E and trajectory Ω per unit volume, energy, and solid angle, and $d\beta = drd\Omega dE$.

The conditional probability density distribution, $P(\beta|\beta')$, is the probability that a particle with energy E and trajectory Ω experiences a collision at r , given that it last entered collision at r' with trajectory Ω' and energy E' . It accounts for the likelihood of attenuation between r' and r , as well as change in trajectory and energy, Ω' and E' , to Ω and E , for each possible collision type.

Equation 3 is a conservation law, stating that the only source of n th scattered particles at r with energy E and direction Ω are $(n - 1)$ th scattered particles scattering into the state (Ω, E) somewhere along the

line $r' = r - \Omega \cdot R$. Since the probability that a particle experiences its n th collision at β depends only on its state, β' , leaving its previous collision, radiation transport is a Markov process. Thus, the solution, $\Phi(\beta)$, to any transport problem is equivalent to the set of all possible random walks through β -space.

2.2 Computational methods

Direct solution of Eq. 3 for problems of practical interest by conventional numerical or analytic means is not possible because of the large number (six) of independent variables necessary to describe particle fluence. Two classes of numerical methods are currently available for solving the transport equation: deterministic and Monte Carlo methods. Deterministic approaches, such as the discrete ordinates method, involve discretizing some or all of the energy, spatial, or angular variables. As of this writing (6), these approaches have not been successfully used to solve problems involving three-dimensional, heterogeneous geometries. Monte Carlo simulation (5, 6) is therefore the method of choice for solving complicated transport problems. In essence, the method consists of randomly choosing a small number of particle trajectories or histories from the set of all those possible. The quantity of interest is then averaged over this small set giving a statistical estimate of the solution. In exchange for the capability of treating geometrically complex arrangements of ionizing radiation sources and absorbers, the precision of a deterministic solution is sacrificed.

This approach has been extensively applied to both photon and electron transport problems of clinical interest in the last few years. In following sections, the principles of photon and electron transport by Monte Carlo simulation will be reviewed.

3.0 MONTE CARLO SIMULATION

3.1 Random sampling

As noted above, Monte Carlo simulation consists of constructing, by means of a digital computer, a randomly selected set of particle trajectories. For each history, this amounts to making a sequence of independent random choices corresponding to significant events in the life of the ionizing particle. These random decisions include: selecting the point of origin, initial energy, and trajectory of the primary particle from its source distribution, selecting the distance traversed to first collision, the type of collision experienced, and its trajectory and energy leaving the collision. Each of these steps involves randomly choosing a sample, x^* , from a possibly multi-dimensional probability density function (PDF), $f(x)$. On a

digital computer, the problem of randomly sampling from an arbitrary PDF is reduced to the simpler problem of randomly choosing a uniformly distributed number, r^* , from the unit interval, (0, 1). Both the systematic accuracy and convergence of Monte Carlo estimates require a large supply of such pseudorandom numbers to insure that the underlying sampling procedures are, in fact, random. Thus, no random number generator, including those supplied with computer operating systems, should be used without insuring that it is well understood and thoroughly tested. Many ingenious and clever techniques have been developed (5, 7, 8, 9) to sample PDF's derived from the exponential attenuation law, differential cross sections, and various types of primary particle source distributions.

3.2 Monte Carlo simulation of photon transport

A two-dimensional representation of a typical photon history is shown in Fig. 1. The vector $\beta_j = (r_j, \Omega_j, E_j)$ represents the state of the photon leaving its j th interaction or collision at position r_j with energy E_j and direction Ω_j . Each history α can be represented by a sequence of states of the form $\alpha = (\beta_0, \beta_1, \dots)$. As interactions between the photon and the medium are limited to the discrete points (r_0, \dots, r_j, \dots) , the trajectories connecting these collision sites are straight lines.

Each state β_j is simulated by randomly selecting its values from the probability distribution found in the integral form of the transport Eq. 3. If $j = 0$, β denotes the initial position, direction, and energy of a primary photon which must be sampled from the source distribution function, $S(r, \Omega, E)$. If $j \geq 1$, the photon has scattered at least once, and the new state β_j must be sampled from the conditional PDF, $P(\beta_j | \beta_{j-1})$ as follows:

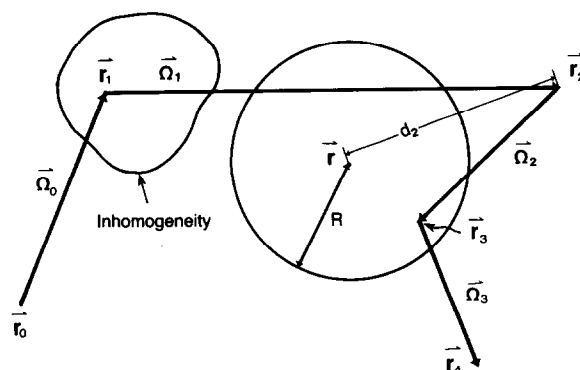
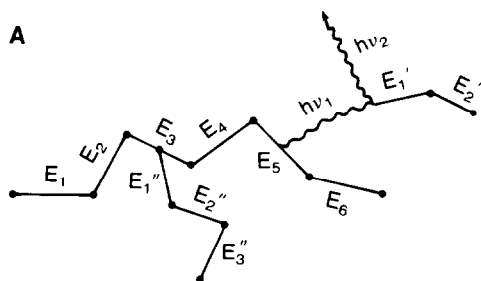


Fig. 1. Two-dimensional representation of a typical photon history. The vector, Ω_j , denotes the trajectory of the photon, leaving its j th collision at location r_j and E_j denotes its energy. (Adapted from reference 10).

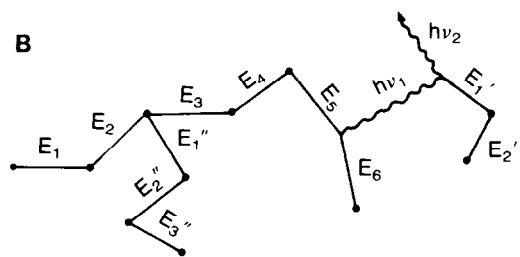
1. Randomly choose distance, s , to next collision at r_j from the PDF $P(s) = \mu e^{-\mu s}$. As illustrated by Fig. (2), complex heterogeneous geometries can be taken into account by summing $\mu \cdot s$ over all regions encountered along the trajectory Ω_{j-1} .
2. Randomly choose the interaction process at j th collision, based upon the relative magnitudes of the total cross sections ($\sigma_{pe}, \sigma_{coh}, \sigma_{inc}, \dots$) of the competing processes (photoelectric absorption, coherent and incoherent scattering, etc.).
3. Sample the PDF, defined by the differential cross section $d\sigma/d\Omega$ for the process chosen in step 2), to find the direction, Ω_j leaving the j th collision.

Both σ and $d\sigma/d\Omega$ depend on the composition of the region containing r_j . This process is repeated until the photon history is terminated by absorption or escapes from the system.

An important component of the simulation is estimation of the contribution, $k(\beta_j)$, made by each simulated collision, β_j , to the quantity of interest (10). Suppose an estimate of the collision kerma,



$$E_{n-1} - E_n = \Delta E \text{ always selected from } f(\Delta E, E_{n-1})$$



$$E_{n-1} - E_n = \begin{cases} (S_n - S_{n-1}) L_\Delta(E_{n-1}) & \text{if multiple scattering} \\ E_1' & \text{if d-ray creation} \\ h\nu_1 & \text{if Bremsstrahlung} \end{cases}$$

Fig. 2. Two-dimensional representation of Class I (A) and Class II (B) condensed electron histories. E_j denotes the energy of the electron at the end of the j th step. Straight lines denote electrons and wavy lines indicate photons. Primed and double-primed trajectories indicate secondary electrons.

$K(r)$, at point r of Fig. 1 is desired. One simple approach is to calculate the energy deposited in a spherical 'detector' region of radius R centered about r :

$$k(\beta_j) = \begin{cases} \frac{3(E_{j-1} - E_j)}{4\pi\rho R^3} & \text{if } |r - r_j| \leq R \\ 0 & \text{if not.} \end{cases} \quad (4)$$

Having simulated a finite set of histories, $(\alpha_i)_{i=1}^N$, an estimate of the kerma based on N histories can be made:

$$\hat{K}(r) = \frac{1}{N} \sum_{i=1}^N \sum_{j=1}^{N_i} k(r_{ij}, \Omega_{ij}, E_{ij}), \quad (5)$$

where the subscript i denotes the history α_i , the subscript j denotes the order of the collision within α_i , and N_i is the number of collisions comprising α_i . It is crucial to recognize that \hat{K} is a statistical estimate of the corresponding "true" value, $\langle K \rangle$, defined by averaging the estimator over the set of all histories specified by the transport equation. The standard deviation σ_k , can be estimated by summing over the finite sample,

$$\sigma_k \simeq \left[\frac{1}{(N-1)} \sum_{i=1}^N \sum_{j=1}^{N_i} [\hat{K} - k(\beta_{ij})]^2 \right]^{1/2}. \quad (6)$$

This parameter is of great practical importance in that it describes the degree of statistical precision achievable by a Monte Carlo estimate for a fixed number of histories N . The relationship between σ_k , N , and statistical precision is given by the central limit theorem:

$$P(|\hat{K} - \langle K \rangle| \leq n \cdot \sigma_k \cdot N^{-1/2}) \simeq \frac{1}{\sqrt{2\pi}} \int_{-n}^n e^{(-x^2/2)} dx. \quad (7)$$

$P(|\hat{K} - \langle K \rangle| \leq n \cdot \sigma_k \cdot N^{-1/2})$ is the probability that the estimate \hat{K} differs from its limiting value $\langle K \rangle$ by no more than $n \cdot \sigma_k / \sqrt{N}$. Equation 7 shows that the Monte Carlo estimate converges slowly with the number of histories, N . For each additional digit of significance, the number of histories must be increased a hundred-fold. The brute force tactic of increasing N to improve precision rapidly reaches the point of diminishing returns. In practice, one aims at reducing the variance per unit of computational effort by altering the scoring and sampling procedures.

Several (11, 12, 13) highly general and extensively benchmarked photon-neutron transport codes are available essentially for free. Each of these codes is capable of simulating highly complex geometries.

3.3 Extension of Monte Carlo techniques to electron transport

The photon transport simulation techniques described thus far assume that energy transferred from

the photon field to the medium is absorbed locally at the simulated collision sites. Thus, such simulations accurately predict absorbed dose only when secondary charged particle equilibrium (CPE) obtains. This assumption is not valid, for example, for megavoltage beams which set into motion secondary charged particles having ranges of up to several centimeters. Absence of CPE gives rise to many clinically significant phenomena such as the dose buildup effect at the phantom surface and dose perturbations at media interfaces and beam edges. Thus, rigorous electron and coupled photon-electron transport calculations are essential for accurate theoretical dosimetry in this energy range.

Because of the large number of collisions (10^5) an electron experiences in slowing down, compared to photons (≈ 30), direct stochastic simulation of all collisions, as is done with photons, is not practical. To overcome this problem, a hybrid approach known as "condensed history Monte Carlo" is used which combines analytical and stochastic elements. Essentially, an artificial random walk is constructed, each step of which includes the combined effect of many collisions as the electron traverses a thin layer of matter. As the methods of implementing this approach will be only briefly reviewed here, the interested reader is referred to Berger's classic review article (14).

A typical condensed history is illustrated by Fig. 2. Within each step, the electron is assumed to lose energy continuously, such that the energy lost is a deterministic function of its total pathlength, s_n , traveled through its n th step. This assumption, the continuous-slowing-down-approximation (CSDA), ignores the fluctuation of energy loss about this mean value caused by random production of δ -rays and Bremsstrahlung photons and the correlation between these energy loss events and the trajectory of the primary electron. For the moment, production of secondary particles will be ignored. Mathematically, the sequence of path lengths, $\{s_j\}$ is defined by

$$s_{j+1} = s_j + \int_{E_j}^{E_{j+1}} [S_{col}(E')]^{-1} dE' \quad (8)$$

where $S_{col}(E)$ is the linear collisional stopping power evaluated at energy E . Usually, a logarithmic energy grid is assumed, by requiring $\Delta E_j = E_{j-1} - E_j$ to correspond to a fixed fraction (0.4% to 10%) of the energy E_{j-1} . Thus, a condensed history can be represented as a sequence of vectors $\beta_j = (r_j, \Omega_j, E_j, s_j)$.

The trajectory, Ω_j , of an electron emerging from the j th step, is randomly selected from one of several available multiple scattering distributions, $P_M(\theta, E, \Delta s)$, where θ is angle between Ω_{j-1} and Ω_j . These dis-

tributions, themselves approximate solutions to the transport equation, give the probability of an angular deflection, θ , of an electron of energy E as a result of many coulombic deflections experienced while traversing a layer of thickness Δs . The Goudsmit-Saunders (15) and Moliere (16) multiple scattering theories are most commonly used.

The results of condensed history simulation, assuming only CSDA energy loss and multiple scattering, are illustrated in Fig. 3 (17) for a 20 MeV electron broad beam incident upon a semi-infinite phantom. Note that the depth-dose curve incorporating simulation of energy straggling and secondary electrons has a less well-defined maximum and a more gradual dose falloff than that calculated by the CSDA-multiple scattering model. These differences are largely due to statistical fluctuations in the energy transferred from primary electrons to matter which are ignored by the CSDA energy transfer model. This phenomenon (14), known as energy straggling, produces significant broadening of the depth dose falloff, increase in practical range, and increase in relative surface dose. In addition, large energy transfers can give rise to either Bremsstrahlung x-rays or high-energy secondary electrons (δ -rays) which can be transported through the system using Monte Carlo techniques as

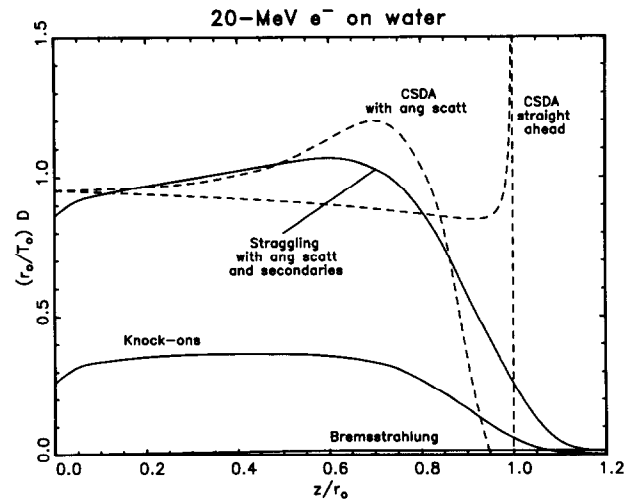


Fig. 3. Central Axis depth-dose for a 20 MeV electron beam as calculated by the ETRAN code assuming various approximations. "Straggling" implies that the energy lost traversing each step is sampled from the Blunck-Leisegang distribution. "Knock-on transport" indicates that simulation of energetic secondary electrons is included as well. The dose distributions arising from secondary electrons ("Knock-ons") and Bremsstrahlung are plotted separately. Note. From "An Overview of ETRAN Monte Carlo Methods for Coupled Electron/Photon Transport Calculations," Proc. 8th Intl. School of Radiation Damage and Protection, Plenum Press.

if they were primary particles. Two different approaches to simulation of energy straggling and transport of δ rays are in common use, which define the two families of coupled photon-electron transport codes available to medical physicists.

The first approach, defining "Class I" codes in Berger's nomenclature, is used by the code ETRAN (18, 19) and its descendents SANDYL, (20) CYLTRAN, (21) ACCEPT (22) and ITS (23). Rather than calculating the energy lost during each multiple scattering step of length Δs from CSDA, ΔE is sampled from the Landau (24) energy straggling distribution, $F(\Delta E, \Delta s, E)$, as modified by Blunck and Leisegang (25). The angular deflection, θ_j , produced by each step is always chosen from the appropriate multiple scattering distribution as described above.

In contrast, Class II codes, most prominently represented by the EGS4 code, (26) combine simulation of discrete collisions with the condensed history approach. For collisions involving energy transfers smaller than some cutoff energy Δ , the CSDA-multiple scattering condensed history approach is used. The pathlength between multiple scattering steps is calculated by Eq. 8 using the restricted stopping power, L_Δ , rather than its unrestricted counterpart, S_{col} . All collisions involving energy transfers to the medium greater than Δ are individually simulated as in photon Monte Carlo, giving rise to a randomly chosen δ rays or Bremsstrahlung photons with trajectories sampled from the appropriate differential cross sections.

Production of secondary electrons and Bremsstrahlung photons is simulated in Class I codes as well. In these codes, creation of a secondary electron modifies neither the energy nor trajectory of the primary electron. These parameters are always sampled from the energy-straggling distribution and multiple scattering distribution, respectively, independently of whether the current step leads to creation of a secondary particle. As in Class II codes, Class I codes require the user to specify a cutoff energy, Δ , below which secondary electrons are assumed to be locally absorbed and above which, energy transfer leads to simulation of secondary particles.

Rogers and Bielajew (27) have made extensive comparisons, for fast electron beams, between EGS4 code (Class II) calculations, ETRAN (Class I) code calculations, and measurements for fast electron beams. As illustrated by Fig. 4, the EGS4 results are in somewhat better agreement with the measured data than the ETRAN calculations. Subsequent investigation (28) has shown that these discrepancies are due to an error in the ETRAN's implementation of the energy-loss straggling algorithm, rather than to

basic differences between physical models assumed by Class I and Class II codes. After fixing this bug, the ETRAN results agree closely with those of EGS4.

Both the ETRAN and EGS4 codes have been extensively benchmarked and are supported by large user groups. No significant physical differences between the modified ETRAN and EGS4 codes in the megavoltage beam energy range are known. The EGS4 user must write his own scoring and geometry routines which affords a great deal of flexibility in tailoring the code to efficiently solve a particular problem. Many such useful subroutines are available for the asking within the EGS user community. In contrast, the most highly developed ETRAN-type codes are integrated "turn-key" packages incorporating a general combinatorial geometry package. Effective operation of either code requires substantial expertise in both basic physics of electron and photon scattering as well as in simulation techniques.

Comparisons between Monte Carlo calculations of central axis depth-dose and measured data are shown for the case of a 15 MV photon beam, in Fig. 5, and for a 20 MeV electron beam in Fig. 4. Note that the buildup of dose at superficial depths characteristic of megavoltage photon beams is reproduced. In general, agreement within a few percent is obtained if scattering from the target, flattening filter, and jaws for photons and the effects of scattering foils, applicators, and intervening air column for electrons, are included.

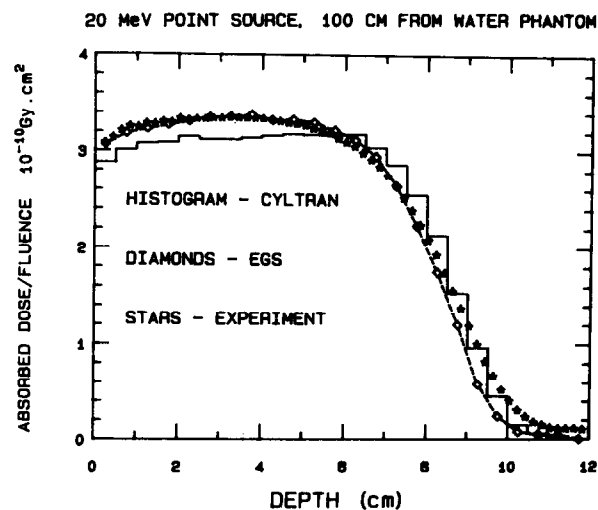


Fig. 4. Comparison of central axis depth dose for a 20 MeV electron beam as measured, calculated by EGS4, and calculated by CYLTRAN. Note. From "Differences in electron depth-dose curves calculated with EGS and ETRAN and improved energy-range relationships," Med. Phys. 13:687-694; 1986.

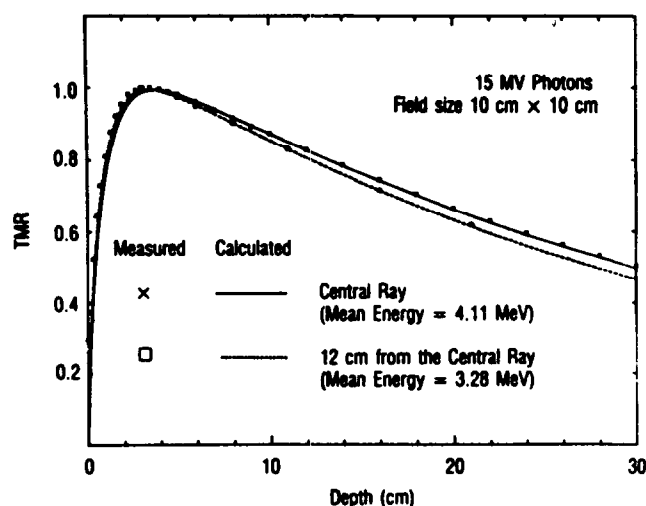


Fig. 5. Central axis and off-axis tissue-maximum ratios for 15 MV X-rays, as calculated by the EGS4 code and as measured. Note. From "Energy and angular distributions of photons from medical linear accelerators," Med. Phys. 12:592-597; 1985.

4.0 APPLICATIONS OF TRANSPORT CALCULATIONS TO TREATMENT PLANNING

Currently, rigorous solutions of the transport equation cannot be used directly to perform routine treatment planning dose calculations. Deterministic calculations can not handle the complex geometries required and the extensive computing resources required by Monte Carlo precludes its use as a patient-specific treatment planning aid. Nevertheless, transport theory is indirectly responsible for many of the most promising new developments in treatment planning dosimetry. A few of the most important generic uses of transport theory in treatment planning are listed.

1. Approximate solutions to the transport equation can form the basis of semianalytic dose computation models, a strategy that has dominated recent developments in electron beam treatment planning.
2. Monte Carlo simulations can be used to perform parametric studies, often difficult or impossible to implement experimentally, which result in valuable explanatory insights.
3. Accurate Monte Carlo calculations are of great value as benchmark data for validating simpler dosimetric models.
4. Unlike empirical measurement, Monte Carlo methods can be used to prospectively calculate absorbed dose within a complex treatment or

beam generation geometry and is a useful tool for designing collimators and other beam modifying accessories.

5. Perhaps the most important current application of the Monte Carlo method, is calculation of basic treatment planning data which, in principle or in practice, is inaccessible to measurement.

Several examples of the value of transport theory, in general, and Monte Carlo calculations, in particular, to treatment planning will be described.

4.1 Electron beam treatment planning

The first practical solution of the electron transport equation was obtained by Spencer (29) using the method of moments (29, 30). This semianalytic method permits calculation of the dose distribution about monodirectional planar and isotropic point sources in an infinite medium. Although continuous energy loss and multiple scattering are rigorously modeled, this approach cannot be generalized to solve problems involving three dimensional geometries or bounded, heterogeneous media. The moments method was first used by Kessaris (31) to calculate broad beam depth-doses for megavoltage electron beams.

Because of the geometric limitations imposed by semianalytic approaches such as the moments method, nearly all rigorous theoretical studies of relevance to treatment planning have been based upon the Monte Carlo method. One of the earliest Monte Carlo studies of energy deposition in water by fast electrons was published by Berger (18). A more recent study by Berger and Seltzer (32) demonstrates the explanatory power of Monte Carlo studies. Figure 6 demonstrates the influence of scattering foil thickness and composition on the central-axis depth dose profile for a 10 MeV electron beam. The utility of Monte Carlo as a design tool has been convincingly demonstrated by Weinhaus et al. (33). The dose distribution within 20 MeV and 30 MeV electron beams in the presence of a longitudinal magnetic field was calculated. They demonstrated (Fig. 7) that by using a magnetic field of appropriate geometry and strength, the dose gradient near the beam edges and distal to the depth of maximum dose could be significantly increased. A dramatic increase in the peak-to-entrance dose ratio, similar to the Bragg peak characteristic of heavy charged particle beams, was also demonstrated.

Approximate analytical solutions of the transport equation have had significant impact on clinical electron beam treatment planning, giving rise to the "pencil beam" family of algorithms (34, 35, 36). The

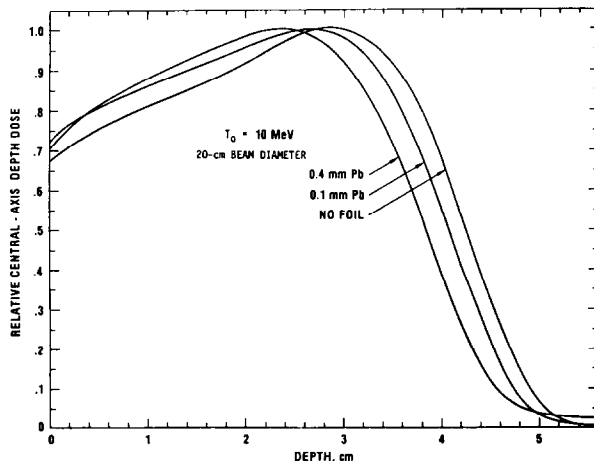


Fig. 6. Depth-dose curves for a 10 MeV electron beam calculated by the ETRAN code for various types of scattering foils. Note. From *Influence of Scattering Foils on Absorbed Dose Distributions from Electron Beams*. Report No. NBSIR 78-1552, National Bureau of Standards, Washington, D.C.; 1978.

main idea (Fig. 8) behind these models is to represent the dose, $D(x, y, z)$, at any point (x, y) and depth z in a phantom arising from an electron beam of arbitrary shape, as the weighted sum, or convolution, of elementary zero-area monodirectional sources, commonly called "pencil beams":

$$D(x, y, z) = \int_{-B}^B \int_{-A}^A S(x', y') K(x - x', y - y', z) dx' dy'. \quad (9)$$

The function $S(x, y)$ denotes the relative source strength at point (x, y) on the phantom surface and $K(x, y, z)$ is the dose at (x, y, z) arising from a single pencil beam normally incident at $(0, 0, 0)$. Calculations based upon this approach in the presence of two- and three-dimensional inhomogeneities and highly oblique incidence are in far better agreement with measured data than the older broad-beam computation techniques which completely ignore the lateral extent of heterogeneities (37).

The function $K(x, y, z)$ can be derived from the Boltzmann transport equation by invoking a series of simplifying assumptions as described by Brahme (38). First, interactions between electrons and matter are limited to continuous energy loss and elastic scattering, giving rise to the Spencer-Lewis equation (30, 39). Next, angular deflections are assumed to be small, resulting in a simplified differential equation first solved by Fermi (40) and subsequently generalized to include energy loss by Eyges (41). Penetration of electrons through matter is characterized by a single material- and energy-dependent parameter related to the linear angular scattering power, $(d\theta^2/dz)$.

The solution of the Fermi-Eyges equation for a monodirectional beam source can be written (34, 36) as

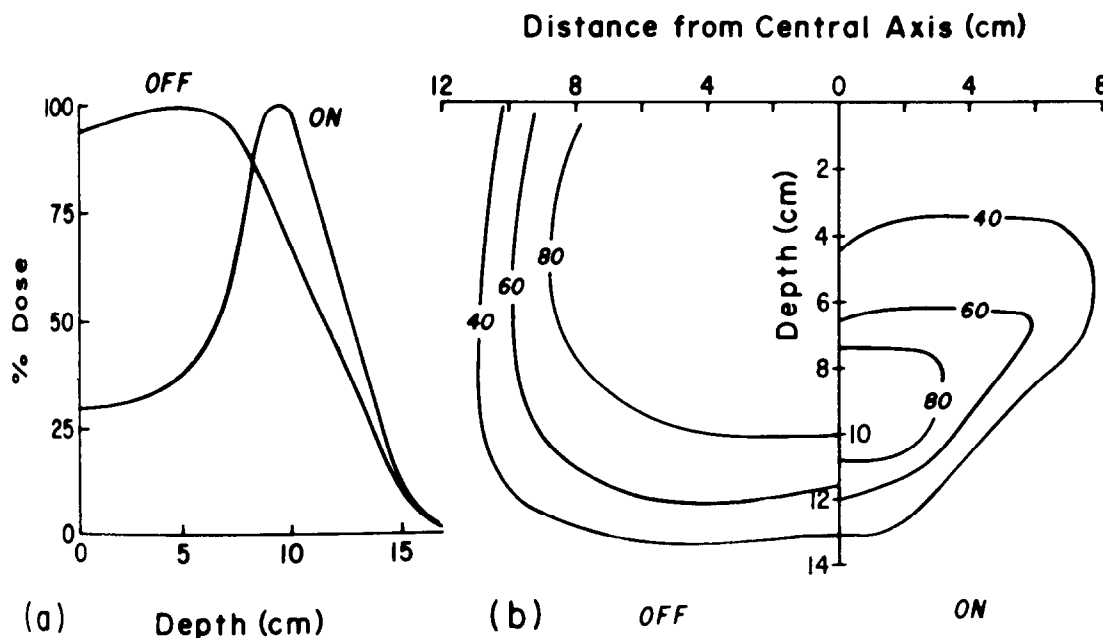


Fig. 7. 30 MeV electron beam central axis depth-dose and isodose curves, as calculated by Monte Carlo with (on) and without (off) a 5.9 T longitudinal magnetic field. Note. From *Enhancement of electron beam dose distributions by longitudinal magnetic fields: Monte Carlo simulations and magnet system optimization*, Med. Phys. 12:598-603; 1985.

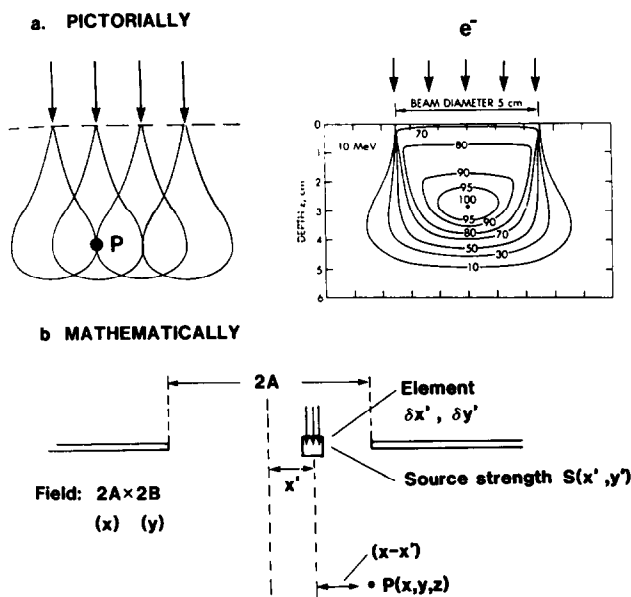


Fig. 8. Pictorial representation of the pencil beam algorithm for electron beam dosimetry. Convolution over elementary point-monodirectional sources to form a broad beam is illustrated in (a). Contribution of a pencil incident at x' to point P at lateral distance x from central axis and depth z is shown in (b). Note. From "The M.D.A.H. Pencil-Beam Algorithm," In *The Computation in Electron Beam Radiotherapy*, edited by Alan Nahum, University of Umea, 1985.

$$K(x, y, z) = \frac{D^\infty(z)}{2\pi\sigma^2(z)} \cdot \exp\left(-\frac{x^2 + y^2}{2\sigma^2(z)}\right) \quad (10)$$

where

$$\sigma^2(z) = \frac{1}{2} \int_0^z (z-u)^2 \frac{d\theta^2}{dz}(u) du$$

and $D^\infty(z)$ is the measured depth-dose for a broad beam. This solution can be generalized to include one-dimensional heterogeneous slab geometries, in which the medium composition varies only with depth z .

Strictly speaking, the heterogeneous pencil beam solution assumes that at any given depth, the medium is homogeneous across the width of the pencil. To evaluate the convolution integral (42) for heterogeneous geometries, it is assumed that, at any depth, the material traversed by the central ray of each pencil extends laterally across that pencil. Clinically, this assumption is approximately true at shallow depths for which the effective width of the pencil is small, allowing absorbed dose to be calculated with reasonable accuracy about heterogeneities smaller than the width of a clinical beam. Storchi and Huizenga (43) have described an iterative numerical algorithm

which allows the angular scattering power to depend on x and y as well as z . Thus, pencil beam distributions $K(x, y, z)$, corrected for variation in medium composition across the width of the pencil beam can be calculated. Using this result in Eq. 9 facilitates more accurate dose estimates near media interfaces.

The Fermi-Eyges theory leads to simple Gaussian beams which ignore large angle scattering, δ ray and Bremsstrahlung production, and the influence of electron loss on the spatial spread parameter, $\sigma(z)$, at large depths. To avoid these limitations, Berger and Seltzer (44) and Lax et al. (45) have used Monte Carlo simulation to calculate the dose distribution for pencil beam sources incident upon a semi-infinite phantom. The agreement between the convolution model (Eq. 9) and measured depth-dose data for small field sizes (see Fig. 9) is significantly improved when pencil beam data derived from Monte Carlo simulations, rather than Fermi-Eyges theory, are used. Direct measurement of pencil beam dose distributions is difficult since the collimation required to produce small diameter beams distorts the results (45).

Rogers et al. (47, 48) have used the EGS4 code to calculate the dose distribution for 10 MeV and 20 MeV electron beams in the presence of standard one-, two-, and three-dimensional aluminum and air

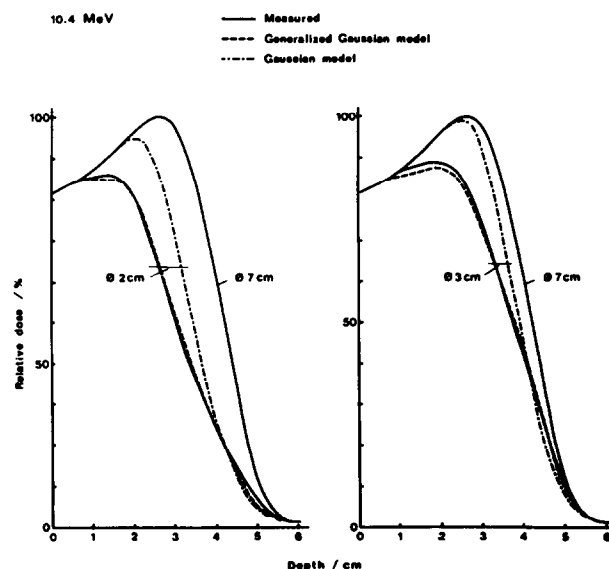


Fig. 9. Pencil beam calculations for 2 cm and 3 cm diameter fields based upon the Fermi-Eyges model (---) and on point-monodirectional beams generated by Monte Carlo simulation (or Generalized Gaussian) (---). For comparison the 7 cm diameter broad beam depth-dose is also indicated. Note. From *Development of a Generalized Gaussian Model for Absorbed Dose Calculation and Dose Planning in Therapeutic Electron Beams*, Ingman Lax, Stockholm, 1986.

inhomogeneities. Figure 10 (47, 48) shows the central axis results for 10 MeV electrons with 1 cm diameter air and aluminum cylinders. Note that the hot and cold spots are much more intense than predicted by the 2-D pencil beam algorithm as implemented by Hogstrom (34). Improved accuracy is expected from more general pencil beam algorithms, Storchi et al. (43).

4.2 Photon beam treatment planning

One of the earliest investigations of photon treatment beam characteristics using Monte Carlo methods was published by Bruce and Johns in 1960 (49). Their photon transport code was used to calculate energy spectra in water, hydrogen, and aluminum for parallel circular beams of photons ranging in energy from 50 KeV to 1.25 MeV. In addition, depth-dose and backscatter factors were derived from this data and compared to experimental measurements. Even though transport of secondary electrons was ignored, the agreement between calculated and

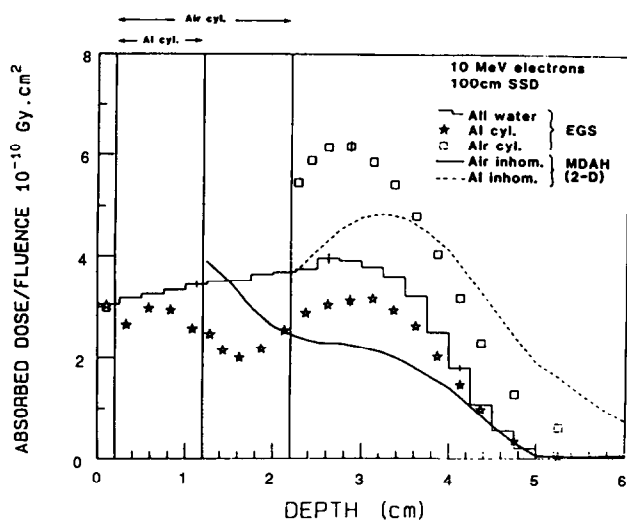


Fig. 10. Central axis dose per unit fluence as calculated by Monte Carlo for a 10 MeV electron beam incident upon a homogeneous water phantom (histogram), with a 1 cm diameter by 2 cm long air cavity embedded in the phantom along central axis (squares), and with a 1 cm diameter by 1 cm long aluminum cylinder (Stars) embedded in the phantom. The solid and dotted lines indicate the predictions of the two-dimensional pencil beam algorithm using Gaussian beams (note the interchange of the air and Al curves). Note. From "Monte Carlo Calculations of Electron Beams in Standard Dose Planning Geometries," in *Proc. 8th Intl. Conf. on the Use of Computers in Radiation Therapy*, Toronto, Canada July 1984. IEEE Computer Society Press, Silver Spring, MD and "Monte Carlo Transport Simulation II. Application to Dose Planning" In *The Computation of Dose Distributions in Electron Beam Radiotherapy*, edited by Alan Nahum, University of Umea, 1985.

measured TAR values for ^{60}Co was 2% to 3%. Other early studies include those of Webb et al. (50, 51) who used Monte Carlo photon transport calculations to study ^{60}Co and 6 MV x-ray dose distributions in the presence of tissue heterogeneities. Their code included an approximate treatment of secondary electron transport based upon the CSDA, straight-ahead approximation. Finally, Burger et al. (52) used transport calculations to calculate neutron depth-dose data in an inhomogeneous slab phantom. They used both a two-dimensional discrete ordinates code and Monte Carlo calculations. The deterministic code produced good agreement with the Monte Carlo estimates but was far more computationally efficient.

The earliest simulation, known to the author, of a treatment machine head that included transport of secondary electrons, is that of McCall et al. (53). Using the EGS code to simulate the transport of electrons incident upon an idealized target and flattening filter assembly, they studied the influence of target and filter composition and thickness on the average energy of the resultant Bremsstrahlung photons. The results of this study were used to improve the depth-dose and off-axis characteristics of the Clinac-35 linear accelerator. Petti et al. (54) used the EGS code to model, in detail, the treatment head of a Clinac-35 accelerator as illustrated by Fig. 11. Their aim was to assess the influence of contaminant electrons, originating in the treatment head, on depth-dose curves in the buildup region. To obtain depth-dose estimates with good statistical precision while using a reasonable amount of computing time, this complex simulation was performed in two stages. First, the treatment head geometry was simulated, utilizing 220,000 primary electrons incident upon the target, from which the distribution of electrons and photons at the phantom surface with respect to energy, angle, and off-axis distance was derived. This was followed by a second simulation which tracked primary photons and electrons, randomly chosen from these distributions, through the phantom geometry. A sample of their results is shown in Fig. 12, clearly demonstrating the effect of contaminant electrons on the buildup of dose. Mohan et al. (55) have used the EGS code to calculate the angular distribution of primary and scattered photons emerging from the treatment heads of a variety of linear accelerators (Fig. 13). These narrow, forward-peaked distributions indicate the deviation of the photons from the radially outward direction caused by scattering processes as they emerge from the head. This study illustrates the great potential of Monte Carlo simulation to calculate machine-specific treatment planning data.

The availability of sophisticated transport calcu-

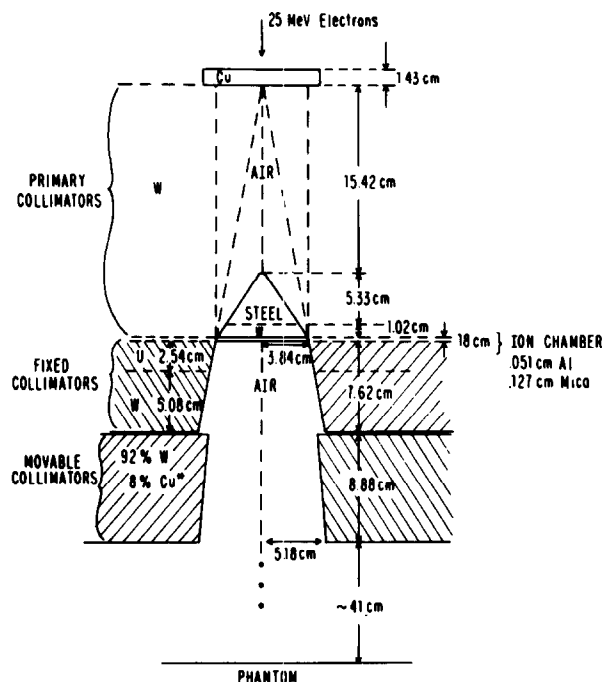


Fig. 11. Geometric model of a Clinac-35 treatment head assumed by the simulation study of Petti (54) et al.

lations has given rise to a new family of photon dose computation algorithms variously called the convolution method, (56, 57) the dose-spread array method

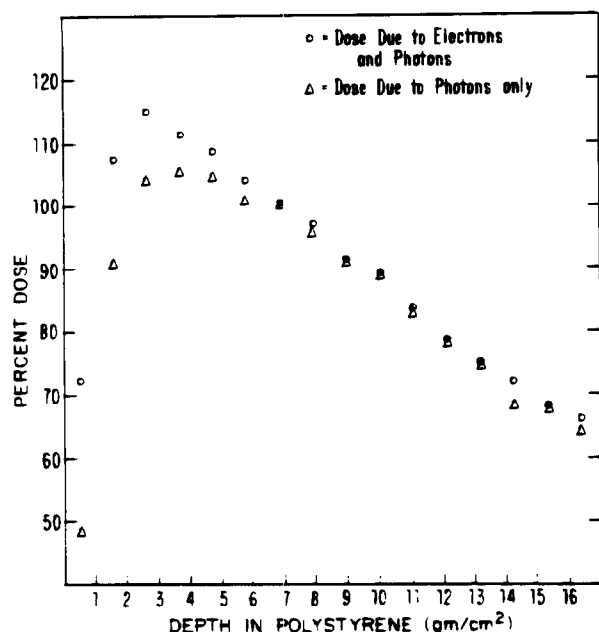


Fig. 12. Depth-dose curve for a Clinac-35 25 MV X-ray beam, as calculated by Monte Carlo, with (circles) and without (triangles) contaminant electrons. Note. From "Investigation of buildup dose from electron contamination of clinical photon beams," Med. Phys. 10:18-24; 1983.

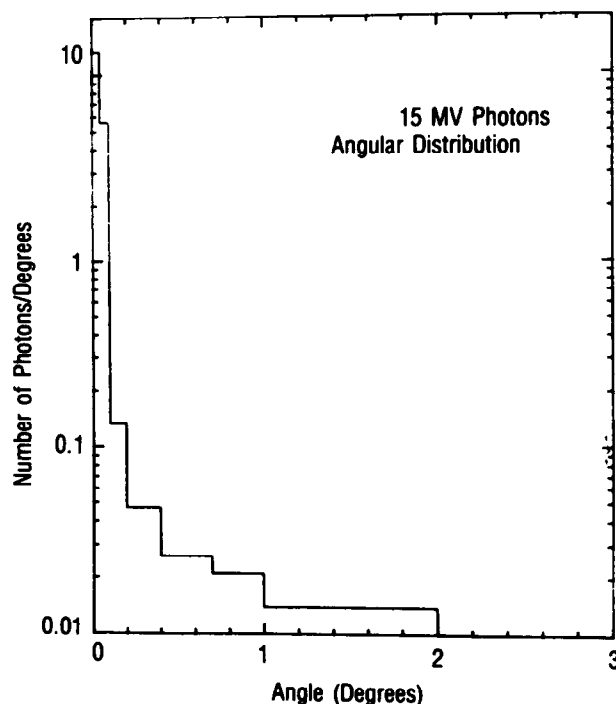


Fig. 13. Angular distribution, relative to the line from target center to point of incidence on the phantom, of photons emerging from a Clinac-20 treatment head operated at a nominal accelerating potential of 15 MV. Note. From "Energy and angular distributions of photons from medical linear accelerators," Med. Phys. 12:592-597; 1985.

(57) and the differential pencil beam model (58) by its developers. Unlike conventional approaches, these methods incorporate both the effects of photon scatter and secondary electron transport. Thus, these models are able to reproduce dosimetric phenomena associated with absence of secondary electron equilibrium near phantom surfaces, beam edges, and media interfaces. It is likely that this computational approach will facilitate more accurate and physically realistic modeling of photon dose distributions in the presence of three-dimensional heterogeneities than is achievable by traditional heterogeneity correction algorithms.

The basic method is illustrated by Fig. 14. The basic data required is a dose-spread array, or scattering kernel, $K(t, \theta)$, which gives the absorbed dose at distance, t , and angle θ , arising from a single primary photon collision at $t = 0$ with an initial trajectory $\theta = 0$. Figure 15 illustrates a scattering kernel for a monoenergetic 10 MeV photon beam. The kernel, $K(t, \theta)$, which has the units of cGy per primary photon collision, is calculated once and for all by Monte Carlo simulation or other theoretical solution of the transport equation assuming an infinite homogeneous medium. Unlike electron pencil beams, $K(t, \theta)$

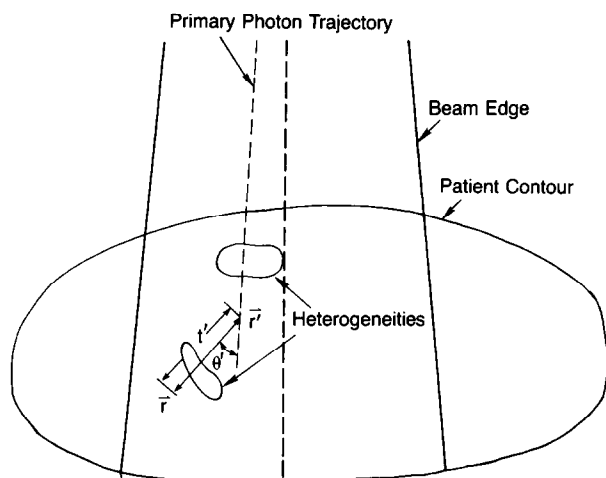


Fig. 14. Geometry of the convolution method of dose calculation where r denotes the point of interest. The variables r' , t' , and θ' used in Eq. (11) are illustrated.

cannot be measured, even in principle, since a zero-area monodirectional source that always experiences its first collision at a fixed point cannot be duplicated experimentally. For a homogeneous phantom, the dose, $D(r)$, can be calculated by convolving K against the primary particle fluence, $\Phi(r')$,

$$D(r) = \int_V \Phi(r') \cdot \mu(r') \cdot K(t', \theta') dV' \quad (11)$$

where μ is primary photon linear attenuation coefficient at r' , $t' = |r - r'|$, θ' is the angle between $(r - r')$ and the primary photon trajectory, and V denotes integration over the entire irradiated volume. Note that the value of $K(r' - r)$ is assumed to be indepen-

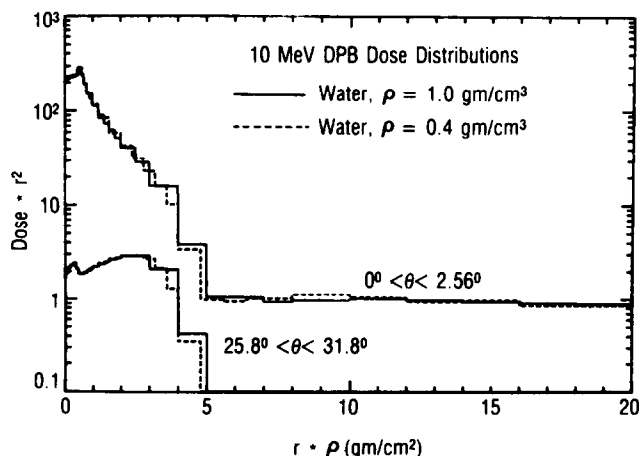


Fig. 15. Plot of the scattering kernel, $K(r, \theta) \cdot r^2$ as a function of distance for fixed angles for a primary photon with energy of 10 MeV. Note. From "Differential pencil beam dose computation model for photons," Med. Phys. 13:64-73; 1986.

dent of the absolute positions, r and r' (i.e., K is spatially invariant).

Dose perturbations arising from patient contour boundaries and air-filled voids surrounded by tissue-equivalent medium are taken into account by Eq. 11 by setting $\Phi \cdot \mu$ to zero within these regions and appropriately scaling the dose-spread array when the path $r - r'$ intersects a void. Figure 16 shows the results of applying Eq. 11 to a "quarter" infinite phantom, demonstrating the ability of the convolution algorithm to accurately model the lateral build-up effect near beam edges. Equally impressive performance of the model in the presence of a slab heterogeneity, consisting of air, is illustrated by Fig. 17. Extension of the convolution algorithm to encompass heterogeneities of arbitrary density and atomic composition, such as lung tissue and metallic prostheses, is an area of active investigation. In principle, such heterogeneities can be approximately treated by appropriately scaling the kernel, K , and by correcting the primary fluence, $\Phi(r')$, for any inhomogeneous regions traversed by the primary photons which induce collisions at r' . However, the optimum scaling algorithm and the ultimate accuracy achievable are not yet known. Figure 15 shows $K(t, \theta)$ as a function of t for fixed θ in the case of a 10 MeV photon beam, demonstrating that $t^2 \cdot K(t, \theta)$ scales with electron density, ρ_e , within an homogeneous medium of fixed composition.

At this point, it is clear that the convolution algorithm performs quite accurately in a number of circumstances. Although computation times are very long compared to commercially-available treatment planning programs, the convolution algorithm is

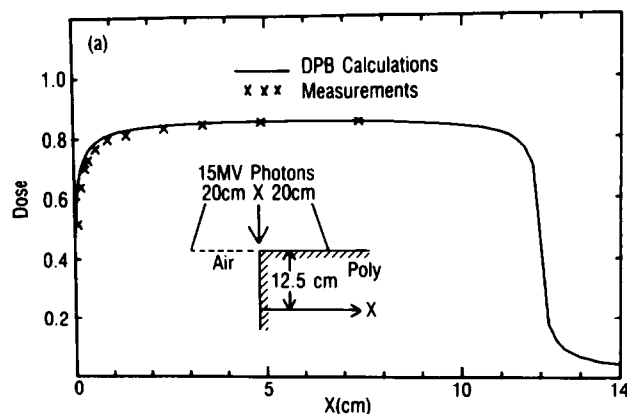


Fig. 16. Comparison of convolution algorithm results (—) with measured results (crosses) for 15 MV X-rays incident upon a quarter-infinite phantom. Note. From "Differential pencil beam dose computation model for photons," Med. Phys. 13:64-73; 1986.

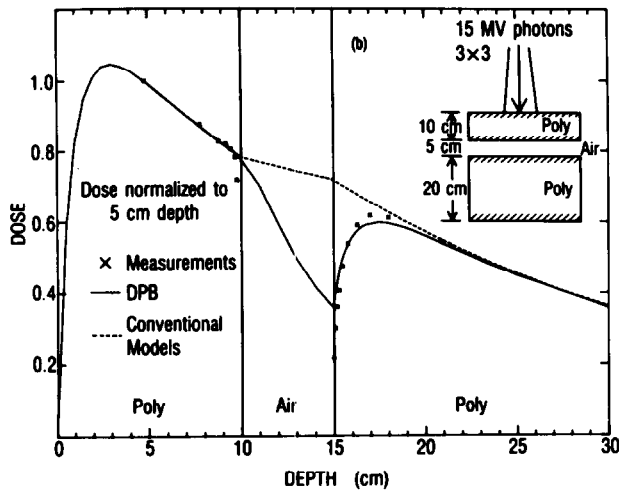


Fig. 17. Comparison of convolution algorithm results (—) with measured results (crosses) for a small 15 MV X-ray beam incident upon a phantom with air slab at 10 cm depth. Note. From "Differential pencil beam dose computation model for photons," Med. Phys. 13:64-73; 1986.

orders of magnitude faster than direct Monte Carlo simulation. Moreover, it can take advantage of vector machine architecture for further acceleration of computing speed.

4.3 Brachytherapy treatment planning

Unlike external beam dosimetry, brachytherapy dosimetry, throughout its history, has relied almost exclusively on calculated, rather than measured, dose distributions. Dose-rate tables for various types of radium sources and dose-calculation formalisms were first described by Sievert (59) in 1921 and Quimby in 1922 (60). At least partially responsible for this trend, are the difficulties inherent in performing accurate dose measurements about brachytherapy sources. Because of the steep dose gradients encountered in the vicinity of interstitial sources, the accuracy achievable by experimental methods is limited (61). Measured data are influenced by detector positioning errors and averaging of dose over the detector volume. The latter problem is especially severe for insensitive detectors such as ion chambers. More sensitive detectors, such as photographic film and various solid state devices, have been used to minimize these artifacts. However, these detectors have a nontissue-like energy response and do not lend themselves to accurate prediction of absolute dose.

To this day, the Sievert integral (59) is almost universally used to calculate dose-rate distributions about filtered ^{198}Au , ^{137}Cs , ^{192}Ir , and ^{60}Co sources. A generalization (62) of this well-known dosimetric model, applicable to extended volume sources illus-

trated by Fig. 18, will be discussed. The algorithm consists (62, 63, 64) of partitioning the extended active source into a set of point sources to each of which inverse square law, filtration correction factors, and corrections for scattering and attenuation in tissue, are separately applied.

The dose-rate, $\dot{D}(r)$ ($\text{cGy} \cdot \text{h}^{-1}$), at point r of Fig. 18 is

$$\dot{D}(r) = c \cdot S_K \cdot (\overline{\mu_{en}/\rho})_{\text{air}}^{\text{wat}} \times \frac{\int_V \rho(r') \cdot F(r-r') \cdot T(\lambda_3) \cdot |r-r'|^{-2} \cdot dV'}{|r_c|^2 \cdot \int_V \rho(r') \cdot F(r_c-r') \cdot |r_c-r'|^{-2} \cdot dV'} \quad (12)$$

The function F contains corrections for absorption and scattering of photons by the active source and filter materials:

$$F(r-r') = \exp\left(-\sum_{j=1}^{N-1} \lambda_j \cdot \mu_j\right) \quad (13)$$

where

$$\sum_{j=1}^N \lambda_j = |r-r'|$$

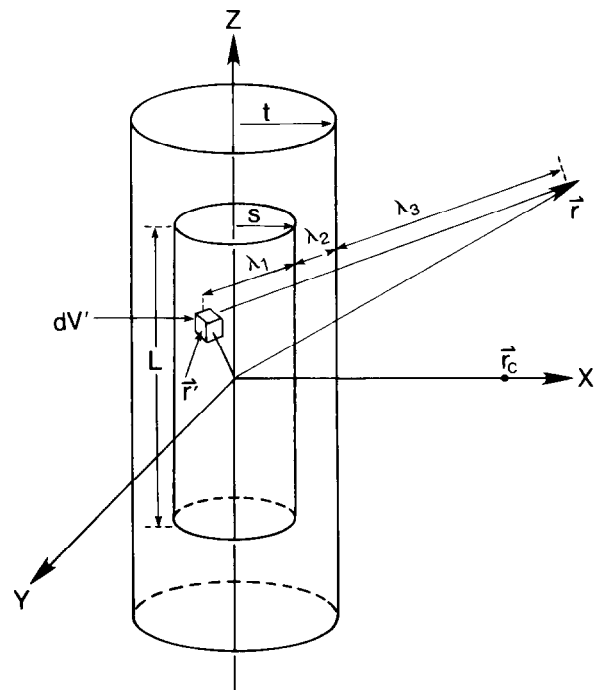


Fig. 18. Schematic view of an intracavitary source. The radioactivity is assumed to be uniformly distributed in a cylindrical region of volume V , length L , and radius s which is concentrically and symmetrically placed in a larger cylinder of radius t , which denotes the source capsule. The symbol dV' represents differential volume element located at r' . An unbounded homogeneous medium is assumed to surround the source.

and the variables λ_1 , λ_2 , and λ_3 represent the linear thicknesses of active core, filter, and surrounding water medium encountered along the ray path extending from r' to r . The other symbols in Eqs. 12 and 13 are defined as follows:

V = volume of active source (region 1).

S_K = strength of the source in terms of the quantity air-kerma strength. The source output, in terms of air-kerma rate in free space (3, 65), is measured at the point $r_c = (d, 0, 0)$.

$(\mu_{en}/\rho)_{air}^{wat}$ = ratio of mass energy absorption coefficients, averaged over the source spectrum in free space, for water to that of air.

$$T(r) = \left. \frac{\text{dose in water}}{\text{water kerma in free space}} \right\} \begin{array}{l} \text{at distance } r \\ \text{from a point} \\ \text{source} \end{array}$$

$\rho(r)$ = density ($\text{Bq} \cdot \text{m}^{-3}$) of radioactivity at point r .

$c = 1.00 \text{ cGy} \cdot \text{cm}^2 / \mu\text{Gy} \cdot \text{m}^2$ is a constant needed to convert the kerma and distance units used by the source strength specification quantity, S_K , to units of centigray and centimeter, respectively.

If the radioactivity is assumed to be distributed along the axis of the inner cylinder of Fig. 18, Eq. 1 reduces to the familiar Sievert line-source integral (e.g., reference 66) used almost universally in intracavitary treatment planning.

Transport calculations are most commonly used in brachytherapy dosimetry to provide input data for the Sievert integration model. The earliest published contribution of this kind was a calculation of scatter and attenuation factor, $T(\lambda)$, for point radionuclide sources in an infinite water medium (67). The method of moments (68) was used to solve the photon transport equation describing this problem. The frequently-cited data of Meisberger et al. (69) are based upon a review of both calculated and measured attenuation and scatter factors.

Despite the obvious advantages of Monte Carlo simulation in dealing with the artifacts associated with brachytherapy dose measurements, this technique has only recently been applied to geometrically complex brachytherapy problems. The present author (64) first used Monte Carlo simulation to evaluate the accuracy of the Sievert model for ^{226}Ra and ^{192}Ir sources suspended in free space. This study showed large discrepancies (5% to 200%) between the Sievert and Monte Carlo calculations for low energy ($\leq 500 \text{ KeV}$) sources encapsulated in high atomic number media. For clinical sources, specified in

terms of measured output along the transverse axis, the Sievert integral was shown to overestimate dose in free space by 3% to 23% near the longitudinal axis of the source and within 2% elsewhere.

The simulation described above was used to calculate the filtration correction factors, described in terms of effective attenuation coefficients, μ_i , needed to evaluate Eq. 13. The conventional geometry for measuring filtration corrections, first described by Keyser (70) and Whyte (71) for platinum-encapsulated ^{226}Ra , was simulated. Exposure rate was calculated at a large distance from a filtered source suspended in air along its transverse bisector. This quantity was calculated for cylindrical filters of different radial thicknesses. A radial transmission curve, for ^{137}Cs encapsulated in iron, is illustrated by Fig. 19. Such investigations (62) demonstrated that radial geometry transmission data do not accurately describe oblique filtration characteristic of brachytherapy sources. For example, as illustrated in Fig. 19, axial transmission, calculated along the longitudinal axis of the source as a function of source capsule length, t , for a fixed radius, differs significantly from the radial transmission curve.

Recently, the author has generalized his Monte Carlo calculations to include the effects of scattering and attenuation by tissue and water media (10, 62, 63) around filtered sources. Such calculations were used to critically evaluate the simple model of scattered radiation assumed by Eq. 12. The absorbed dose at r arising from photons emitted by differential volume element dV' (Fig. 18) is assumed to be related

Transmission of Cs-137 Gamma-Rays through Stainless Steel Filters

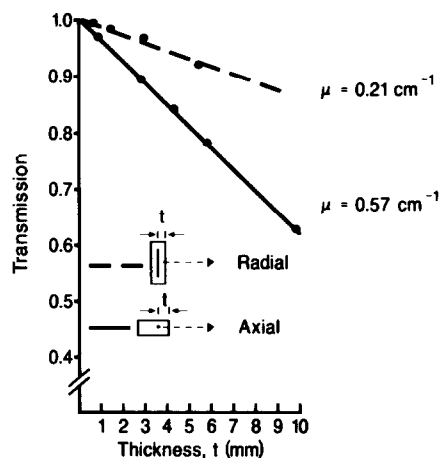


Fig. 19. Transmission of ^{137}Cs Xrays through steel filters of various radii (radial geometry) and through filters of various lengths (axial geometry), all calculated by Monte Carlo. Note the large differences.

to water kerma in free space at that point by the point-source scatter and attenuation factor, $T(\lambda_3)$, which depends only on the distance λ_3 . The counterpart in external beam dosimetry is the assumption that at a given depth, scatter dose is always a fixed fraction of the primary dose, regardless of whether the point of interest lies under a thin filter of large area or under a thick block of small area.

For a ^{137}Cs intracavitary source, consisting of a high-density active core encapsulated in stainless steel, Fig. 20 shows the ratio of absorbed dose in water to water kerma in free space at that point as calculated by the author's photon transport code (62). This ratio is shown as a function of angle with respect to the transverse bisector of the source at a fixed distance of 2 cm from its center. This ratio is approximately unity, as historically assumed (59, 66) at angles well away from the longitudinal axis of source. At points lying within a cone formed by a 15° angle with respect to the longitudinal axis, use of the point source $T(r)$ value underestimates absorbed dose by 4% to 19%. Although increased oblique filtration significantly reduces water kerma in free space, the expected dose deficit is partially offset by radiation

scattered into this region from more intensely irradiated regions of medium. If the cylindrical distribution of radioactivity is replaced by a single point source located at the center of the active source core, the dose-kerma ratio becomes 1.46 at 90° compared to an expected value of 0.993 derived from the point source water attenuation and scatter function, $T(r)$. Dose in water cannot be accurately inferred from water kerma in free space using point-source buildup data in the presence of significant oblique attenuation.

The cumulative effect of the approximations inherent in Eq. 12 gives rise to differences between the Sievert model and Monte Carlo calculations of -9% to -18% near the long axes of clinical ^{137}Cs sources, and 2% agreement elsewhere. By treating the filtration correction as a parameter of best fit, 2% agreement between Monte Carlo and Sievert calculations can be achieved (62).

In comparison to higher energy radionuclides, Monte Carlo calculations have played a larger role in the development of ^{125}I dosimetry. Because of the low energy photons emitted by this radionuclide, the applicability of simple models, such as the Sievert line

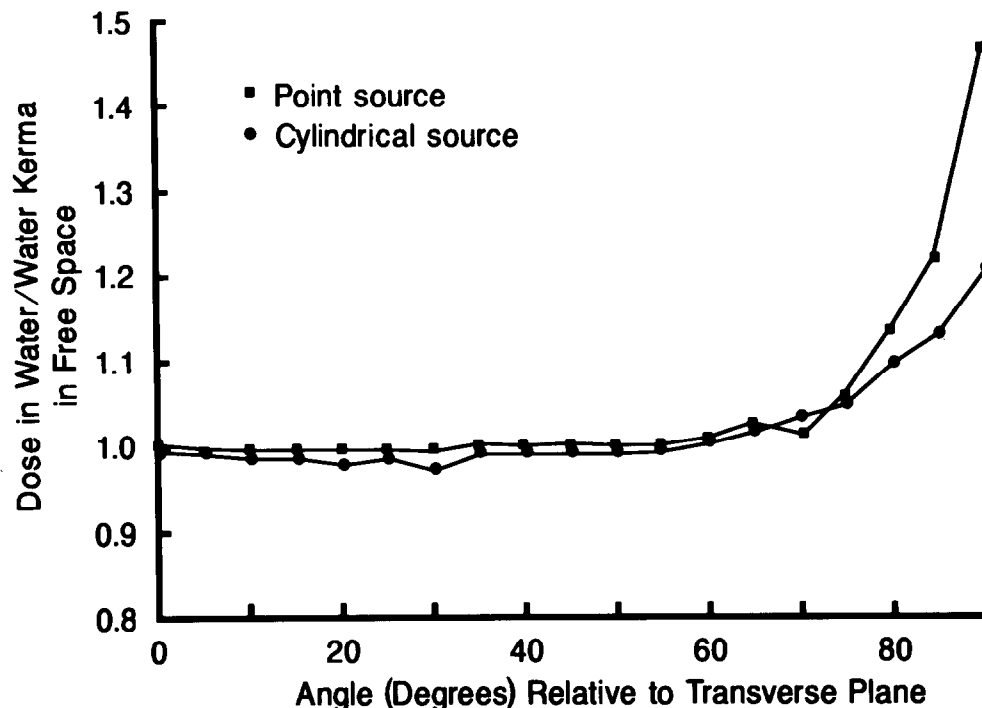


Fig. 20. The ratio of absorbed dose in water at 2 cm from the source center to water kerma in free space at the same point. The data are plotted as a function of angle with respect to the transverse bisector assuming a filtered ^{137}Cs source as illustrated by Fig. 18. A gold active core of 15 mm length and a stainless steel external encapsulation were assumed. The circled data points denote the dose-kerma ratio for radioactivity uniformly distributed throughout the core whereas the square points denote the same ratio for a point source located at the geometric center of the core.

integral, is suspect. In addition, absolute measurement of absorbed dose about such sources is much more difficult than for the higher-energy radioisotopes traditionally used in brachytherapy. Using Monte Carlo techniques, Dale (72) has shown that the specific dose constant of ^{125}I , defined as the dose rate at 1 cm from the source per unit source strength, is sensitive to the composition of the tissue surrounding the source. For example, the dose constant is 45% smaller in fat than in water. Williamson (73) has used Monte Carlo methods to calculate the specific dose constants in water for the three types of commercially available seeds. This study modeled the detailed internal geometry of each seed as well as the measurement geometry used by the National Bureau of Standards to establish an exposure standard for these sources. The results indicate that currently accepted values overestimate dose by 10% to 15% and demonstrate that absolute dose can be estimated by transport calculations. The differences are due to degradation of the ^{125}I spectrum by scattering within the seed and inclusion of low-energy titanium characteristic xrays in the exposure calibration standard. Both Williamson (74) and Chiu-Tsao (75) have used Monte Carlo techniques to calculate the two-dimensional relative dose distribution about ^{125}I seeds in water medium simulating the anisotropic distribution of primary photons arising from the seed construction as well as scattering of photons by the medium.

Theoretical dose calculations applicable to ^{125}I seeds attached to gold plaques for treatment of intraocular malignancies have been described (76, 77). These calculations have taken into account the perturbing influence of the eye plaque, the air-tissue interface imposed by the head contour, and the non-water equivalence of the intraocular fluid.

5.0 SUMMARY AND FUTURE DEVELOPMENTS

Transport theory, both by stimulating development of approximate but physically interpretable models and by providing relatively exact solutions to geometrically complex problems, has made important contributions to clinical dose computation. At least two future developments may be anticipated. As computing hardware becomes more inexpensive and powerful, Monte Carlo calculations will be more frequently used to calculate treatment machine- or source-specific data for treatment planning. Given an enhancement in computing efficiency of 10 to 20 relative to the current generation of VAX mini-computers, patient-specific Monte Carlo treatment planning may even be feasible. Another promising area is

the development of sophisticated discrete ordinates codes (6, 78). Morel and Lorence (79) have successfully adapted a standard one-dimensional discrete ordinates code, originally developed for neutral particle transport, for solving simple electron and coupled photon-electron transport problems. They conclude that this method is as accurate and from 10 to 100 times more efficient than Monte Carlo. Recently, Fillapone (80) has developed a method of generating discrete ordinates scattering matrices for electrons which model, nearly exactly, wide-angle collisions without introducing additional artifacts. This method substantially improves the accuracy and one-dimensional calculations and appears to generalize to two- and three-dimensional geometries.

Further improvements in numerical techniques and in the size of central memory supported by modern mini-computers may make three-dimensional discrete ordinates calculations achievable in principle. These computing techniques could well replace Monte Carlo simulation in certain treatment planning applications.

REFERENCES

1. Milan, J.; Bentley, R.E. The storage and manipulation of radiation dose data in a small digital computer. *Brit. J. Radiology* 47:115-121; 1974.
2. Cunningham, J.R.; Shrivastava, P.N.; Wilkinson, J.M. Program IRREG-calculation of dose from irregularly shaped radiation beams. *Comput. Programs Biomed.* 2:192-199; 1972.
3. International Commission on Radiation Units and Measurements. Radiation Quantities and Units, Report No. 33; 1980, Washington, D.C.
4. Andreo, P. The interaction of electrons with matter II. scattering. In: Nahum, Alan E., ed. *The Computation of Dose Distributions in Electron Beam Radiotherapy*. Sweden: Umea University; 1985; p. 56.
5. Fano, U.; Spencer, L.V.; Berger, M.J. Penetration and diffusion of x-rays. In: Flugge, S., ed. *Encyclopedia of Physics*, Vol. 38, No. 2. Berlin: Springer-Verlag; 1959; pp. 660-817.
6. Lewis, E.E.; Miller, W.F., Jr. *Computational methods of neutron transport*. NY: John Wiley & Sons; 1984.
7. Williamson, J.F. Monte Carlo simulation of photon transport phenomena. In: Morin, R.L., ed. *Monte Carlo Simulation in the Radiological Sciences*. Cleveland: Chemical Rubber Company Press; pp. 53-102; 1987.
8. Hammersley, J.M.; Handscomb, D.C. *Monte Carlo methods*. London: Methuen & Co. Ltd.; 1964.
9. Kahn, H. Random sampling (Monte Carlo) techniques in neutron attenuation problems. *Nucleonics* 6:27-37; 1950.
10. Williamson, J.F. Monte Carlo evaluation of kerma at a point for photon transport problems. *Med. Phys.* 14:567-578; 1987.
11. Emmett, M.B. The morse Monte Carlo radiation transport code system report, No. ORNL-4972, Oak Ridge National Laboratory, Oak Ridge, Tenn., February 1975.
12. Godfrey, T.N.K. MCNP-A general Monte Carlo code for neutron and photon transport, LA-7396-M Rev. 2, J.F. Briesmeister, Ed., Los Alamos National Laboratory, Los Alamos, N.M., Sept. 1986.
13. Lichtenstein, H.; Cohen, M.O.; Steinberg, H.A.; Troubetzkoy, E.Z.; Beer, M. The SAM-CE Monte Carlo System for Radiation Transport and Criticality Calculations in Complex Configurations (Revision 7.0), Computer Code Manual CCM-8,

- Research Project 972, Mathematical Applications Group, Inc., Elmsford, N.Y., July 1979.
14. Berger, M.J. Monte Carlo calculation of the penetration and diffusion of fast charged particles. In: Alder, B.; Fernbach, S.; Rotenberg, M., eds. *Methods in Computational Physics*, Vol. 1, Statistical Physics. New York: Academic Press; 1963: p. 135.
 15. Goudsmit, S.; Saunderson, J.L. Multiple scattering of electrons. *Phys. Rev.* 57:24–29; 1940.
 16. Moliere, G., Theorie der Streuung schneller geladener Teilchen. II. Mehrfach- und Vielfachstreuung. *Z. Naturforsch* 3a:78; 1948.
 17. Seltzer, S.M. An Overview of ETRAN Monte Carlo Methods for Coupled Electron/Photon Transport Calculations. Proceedings of 8th International School of Radiation Damage and Protection, Erice, Italy, 24 September–3 October, 1987, In Press, Plenum Press.
 18. Berger, M.J. Calculations of energy dissipation by electrons in water. *Natl. Bur. Std. U.S., Rept.* 8678, 1965.
 19. Seltzer, S.M. Transmission of electrons through foils. Report No. NBSIR74-457, U.S. Department of Commerce, National Bureau of Standards, Washington, D.C., 1974.
 20. Colbert, H.M. SANDYL: A computer code for calculating combined photon-electron transport in complex systems, (Sandia Laboratories) Report SLL-74-0012; 1973.
 21. Halbleib, J.A., Sr.; Vandevender, W.H. CYLTRAN. *Nucl. Sci. Eng.* 61:288; 1976.
 22. Halbleib, J.A. ACCEPT: A three dimensional electron/photon Monte Carlo transport code using combinational geometry, (USDOE, 1979) Sandia Laboratories Report SAND79-0415.
 23. Halbleib, J.A.; Mehlhorn, T.A. ITS: The integrated tiger series of coupled electron/photon Monte Carlo transport codes, (USDOE, 1984) Sandia Report SAND84-0573.
 24. Landau, L. On the energy loss of fast particles by ionization. *J. Phys. USSR* 8:201–205; 1944.
 25. Blunck, O.; Leisegang, S. Zum energieverlust schneller Elektronen in dünnen Schichten. *Z. Physik* 128:500–505; 1950.
 26. Nelson, W.R.; Hirayama, H.; Rogers, D.W.O. The EGS4 Code System, SLAC-Report-255, Stanford Linear Accelerator Center, 1985.
 27. Rogers, D.W.O.; Bielajew, A.F. Differences in electron depth-dose curves calculated with EGS and ETRAN and improved energy-range relationships. *Med. Phys.* 13:687; 1986.
 28. Rogers, D.W.O. personal communication; 1987.
 29. Spencer, L.V. Theory of electron penetration. *Phys. Rev.* 98:1597–1615; 1955.
 30. Lewis, H.W. Multiple scattering in an infinite medium. *Phys. Rev.* 78:526–529; 1950.
 31. Kessaris, N.D. Calculated absorbed dose for electrons. *Rad. Res.* 23:630–640; 1964.
 32. Berger, M.J.; Seltzer, S.M. The influence of scattering foils on absorbed dose distributions from electron beams, Report No. NBSIR 78-1552, National Bureau of Standards, Washington, D.C., 1978.
 33. Weinhaus, M.S.; Nath, R.; Schulz, R.J. Enhancement of electron beam dose distributions by longitudinal magnetic fields: Monte Carlo simulations and magnet system optimization. *Med. Phys.* 12:598; 1985.
 34. Hogstrom, K.R.; Mills, M.D.; Almond, P.R. Electron beam dose calculations. *Phys. Med. Biol.* 26:445; 1981.
 35. Perry, D.; Holt, G. A model for calculating the effects of small inhomogeneities on electron beam dose distributions. *Med. Phys.* 7:207; 1980.
 36. Werner, B.L.; Khan, F.M.; Deibel, F.C. A model for calculating electron beam scattering in treatment planning. *Med. Phys.* 9:180–187; 1982.
 37. Andreo, P. Broad beam approaches to dose computation and their limitations. In: Nahum, A., ed. *The Computation of Dose Distributions in Electron Beam Radiotherapy*. Umea University, Sweden, 80; 1985.
 38. Brahme, A. Elements of Electron Transport Theory. In: Nahum, A.E., ed. *The Computation of Dose Distributions in Electron Beam Radiotherapy*. Umea University, Sweden, 72; 1985.
 39. Fillapone, W.L. Derivation of a generalized Spencer-Lewis equation. *Trans. Am. Nucl. Soc.* 49:223; 1985.
 40. Rossi, B.; Greisen, K. Cosmic-ray theory. *Rev. Mod. Phys.* 13:265; 1941.
 41. Eyges, L. Multiple scattering with energy loss. *Phys. Rev.* 74:534; 1948.
 42. Nahum, A.E. The M.D.A.H. pencil-beam algorithm. In: Nahum, A.E., ed. *The Computation of Dose Distributions in Electron Beam Radiotherapy*, UMEA University, Sweden, 151; 1985.
 43. Storchi, P.R.M.; Huizenga, H. On a numerical approach of the pencil beam model. *Phys. Med. Biol.* 30:467–473; 1985.
 44. Berger, M.J.; Seltzer, S.M. Tables of Energy Deposition Distribution in Water Phantoms Irradiated by Point Monodirectional Electron Beams with Energies from 1 to 60 MeV, and Applications to Broad Beams, Report NBSIR 82:2451, National Bureau of Standards, Washington, D.C., 1982.
 45. Lax, I.; Brahme, A.; Andreo, P. Electron beam dose planning using gaussian beams: Improved radial dose profiles. *Acta Radiol. Suppl.* 364:49–59; 1983.
 46. Lax, I. Development of a Generalized Gaussian Model for Absorbed Dose Calculation and Dose Planning in Therapeutic Electron Beams, Doctoral Dissertation, Department of Radiation Physics, University of Stockholm, Stockholm, Sweden, 1986.
 47. Rogers, D.W.O.; Bielajew, A.F.; Nahum, A.E. Monte Carlo calculations of electron beams in standard dose planning geometries. In *Proceedings of the Eighth International Conference On the Use of Computers in Radiation Therapy*, Toronto, Canada, July 1984, IEEE Computer Society Press, Silver Spring, MD., pp. 140–144.
 48. Nahum, A.E. Monte Carlo electron transport simulation II. Application to dose planning. In: *The Computation of Dose Distribution in Electron Beam Radiotherapy*, edited by Alan E. Nahum, UMEA University, Sweden, 151, 1985.
 49. Bruce, W.R.; Johns, H.E. The spectra of x-rays scattered in low atomic number materials. *Brit. J. Radiol. Suppl.* 9; 1960.
 50. Webb, S.; Fox, R.A. Verification by Monte Carlo methods of a power law tissue-air ratio algorithm for inhomogeneity corrections in photon beam dose calculations. *Phys. Med. Biol.* 25:225–240; 1980.
 51. Webb, S.; Parker, R.P. A Monte Carlo Study of the interaction of external beam x-radiation with inhomogeneous media. *Phys. Med. Biol.* 23:1043–1059; 1978.
 52. Burger, G.; Morhart, A.; Nagarajan, P.S.; Wittmann, A. Determination of depth dose distributions by means of transport calculations. In: Burger, G.; Broerse, J.J.; Urban; Schwarzenberg, eds. *Treatment Planning for External Beam Therapy with Neutrons*, Munich, pp. 83–92; 1981.
 53. McCall, R.C.; McIntyre, R.D.; Turnbull, W.G. Improvement of linear accelerator depth-dose curves. *Med. Phys.* 5:518–524; 1978.
 54. Petti, P.L.; Goodman, M.S.; Gabriel, T.A.; Mohan, R. Investigation of buildup dose from electron contamination of clinical photon beams. *Med. Phys.* 10:18–24; 1983.
 55. Mohan, R.; Chui, C. Energy and angular distributions of photons from medical linear accelerators. *Med. Phys.* 12:592–597; 1985.
 56. Boyer, A.L.; Mok, E.C. Calculation of photon dose distributions in an inhomogeneous medium using convolutions. *Med. Phys.* 13:503; 1986.
 57. Mackie, T.R.; Scrimger, J.W.; Battista, J.J. A convolution method of calculating dose for 15-MV x-rays. *Med. Phys.* 12:188–196; 1985.
 58. Mohan, R.; Chui, C. Differential pencil beam dose computation model for photons. *Med. Phys.* 13:64–73; 1986.
 59. Sievert, R.M. Die Intensitätsverteilung der primären-Strahlung in der Nahe medizinischer Radium-präparate. *Acta Radiologica* 1:89–128; 1921.

60. Quimby, Edith H. The effect of the size of radium applicators on skin doses. *Am. J. Roentgenol.* 9:671-683; 1922.
61. Boyer, A.L. A fundamental accuracy limitation on measurements of brachytherapy sources. *Med. Phys.* 6:454-456; 1979.
62. Williamson, J.F. Monte Carlo and analytic calculation of absorbed dose near ^{137}Cs intracavitary sources. *Int. J. Radiat. Oncol. Biol. Phys.* 15:227-237; 1988.
63. Williamson, J.F.; Seminoff, T. Template-guided interstitial implants: Cs-137 reusable sources as a substitute for Ir-192. *Radiology* 165:265-269; 1987.
64. Williamson, J.F.; Morin, R.; Khan, F. Monte Carlo evaluation of the Sievert integral for brachytherapy dosimetry. *Phys. Med. Biol.*, 28:1021-1932; 1983.
65. American Association of Physicists in Medicine Specification of Brachytherapy Source Strength, AAPM Report No. 21, Task Group No. 32, American Institute of Physics, New York, 1987.
66. Young, M.E.J.; Batho, H.F. Dose tables for linear radium sources calculated by an electronic computer. *Brit. J. Radiol.* 37:38-44; 1964.
67. Berger, M.J. Energy deposition in water by photons from photons from point isotropic sources. *Journal of Nuclear Medicine* 1(Suppl):15-25; 1964.
68. Spencer, L.V.; Fano, U. Penetration and diffusion of x-rays. Calculation of spatial distributions by polynomial expansion. *Journ. of Res. of Natl. Bur. Standards* 46:448-456; 1951.
69. Meisberger, L.L.; Keller, R.J.; Shalek, R.J. The effective attenuation in water of the gamma rays of gold 198, iridium 192, cesium 137, radium 226, and cobalt 60. *Radiology* 90:953-957; 1968.
70. Keyser, G.M. Absorption corrections for radium standardization. *Can. J. Phys.* 28:301-309; 1951.
71. Whyte, G.N. Attenuation of radium gamma radiation in cylindrical geometry. *Brit. J. Radiol.* 28:635-637; 1955.
72. Dale, R.G. Some theoretical derivations relating to the tissue dosimetry of brachytherapy nuclides with particular reference to iodine-125. *Med. Phys.* 11:176-183; 1983.
73. Williamson, J.F. Monte Carlo evaluation of specific dose constants in water for ^{125}I seeds. In Press, *Med. Phys.*; 1988.
74. Williamson, J.F. Theoretical evaluation of dose distributions in water about models 6711 and 6702 ^{125}I Seeds. *Med. Phys.* 15:686-694; 1987.
75. Chiu-Tsao, S-T.; O'Brien, K.; Sanna, R.; Anderson, L. Monte Carlo dosimetry for model 6711 I-125 Seed. *Med. Phys.* 13:784; 1986.
76. Chiu-Tsao, S-T.; O'Brien, K.; Sanna, R.; Tsao, H-S.; Vialotti, C.; Chang, Y-S.; Rotman, M.; Packer, S. Monte Carlo dosimetry for ^{125}I and ^{60}Co in eye plaque therapy. *Med. Phys.* 13:678-682; 1986.
77. Williamson, J.F. Monte Carlo dosimetry of I-125 ophthalmic plaques. *Radiology* 165(P):317; 1987.
78. Carlson, B.G.; Lathrop, K.D. Transport theory, the method of discrete ordinates. In: Greenspan, H.; Kelber, C.N.; Okrent, D., eds. *Computing Methods in Reactor Physics*, Gordon and Breach, New York, 1969, pp. 167-267.
79. Morel, J.E.; Lorence, L.J. Recent developments in discrete ordinates electron transport. *Trans. Am. Nucl. Soc.* 52:384-385; 1986.
80. Filippone, W.L. A Method for generating "smart" electron scattering matrices. *Trans. Am. Nucl. Soc.* 50:270-272; 1985.
81. Nahum, A.E. Water/air mass stopping power ratios for megavoltage photon and electron beams. *Phys. Med. Biol.* 23:24-38; 1978.

About the Author—JEFFREY F. WILLIAMSON is currently an Assistant Professor of Radiation Oncology and is the head of the Division of Physics at the University of Arizona. He was educated at St. Olaf College and Princeton University and received his Ph.D. in Biophysical Sciences at the University of Minnesota. His research interests include development of Monte Carlo simulation techniques and the physics of brachytherapy.